

Examination of the multitude of signals from the phase transition of a neutron star to a quark starDebojoti Kuzur , Ritam Mallick, * R. Prasad , and Shailendra Singh *Department of Physics, Indian Institute of Science Education and Research Bhopal, Bhopal 462 066, Madhya Pradesh, India*

(Received 14 February 2022; accepted 31 May 2022; published 28 June 2022)

The diverse nature of the signal resulting from the phase transition of a neutron star to a quark star and the corresponding astrophysical observations are studied in the present work. The phase transition process is initiated by a density change at the star's center that deconfines matter, followed by weak combustion to attain absolutely stable strange quark matter. The weak combustion results in the generation of huge neutrino-antineutrino pairs, which annihilate and deposit energy on the star's surface. Structural changes due to the energy loss result in the star's misalignment angle evolution and generate gravitational waves. The energy budget and time signature for the neutrino-antineutrino annihilation are compared with the observed isotropic energy for a short γ -ray burst. The misalignment angle evolves to align with the star's symmetry axis, which leads to the sudden increase or decrease of radio intensity from the pulsar. The corresponding gravitational wave emission, both continuous and burst, also has a unique signature pointing towards astrophysical phase transition.

DOI: [10.1103/PhysRevC.105.065807](https://doi.org/10.1103/PhysRevC.105.065807)**I. INTRODUCTION**

The search for the properties of matter at high density and/or temperature has been investigated for quite some time. The measurement of the properties of matter at high energy and zero chemical potential (zero density) is carried out by heavy-ion collider experiments. It has been established that the quark-gluon plasma state exists at high temperature [1–3]. However, there are still no Earth-based experiments in the high-density sector. To know the properties of matter at such densities, we still rely on astrophysical observation coming from neutron stars (NSs). NSs serve as a natural laboratory for testing matter properties at large densities because of their compactness.

However, the task is difficult as direct observation of NS cores cannot be carried out. Observation of NSs comes only from their surface and what physicists can do is model the star from the core to the surface and then match their observation signatures. Again, modeling the matter properties at high density is still a challenge as *ab initio* calculation fails [4,5]. However, the situation improves daily with new observations coming from different astrophysical detectors. The accurate measurement of massive pulsars, on the one hand [6–8], and the gravitational wave (GW) detection of binary NS mergers (BNSMs), on the other [9], sets a stringent constraint on the equation of state (EoS), which describes matter at such high densities.

One of the debates that has come to the forefront is whether quark matter (QM) exists at NS cores [10–19]. QM at finite densities exhibits different phase structures and different states. One of the popular hypotheses of QM is that it consists of an almost equal number of up, down, and strange quarks, whose energy per baryon is less than that of iron [20–22].

However, there is no direct proof of this conjecture, relying on model parameters. The model of absolute stability of strange QM is based on the thermodynamic bag model (MIT bag model).

QM can be generated in NSs by the deconfinement of nucleons into quarks, and then the weak transition of excess down quarks to strange quarks [21,23–26]. The observed massive pulsars raised the question of whether QM can exist at the core of NSs, which often softens the EoS due to the added degree of freedom. However, including repulsive vector interactions and the color-superconducting quark EoS, massive stars can be generated [27]. The next step in constraining the EoS came from the discovery of binary NS merger GW170817. The tidal deformability measurement put an added constraint on the EoS where a 1.4 solar mass star can have a radius between 11.9 and 13.5 km [9], which more or less ruled out the existence of the so-called strange stars (where the entire star up to the surface is composed of quarks) [15,16,19,28,29]. In stars, QM can exist only at the core. These are the so-called hybrid stars (HSs), whose outer region is still in the hadronic phase. Two types of phase transition (PT) can give rise to such HSs, one where there is an abrupt jump in the density from hadron to quark phase (also known as Maxwell's construction) and another where there is a smooth transition from hadron to quark phase. The latter scenario has a phase where both quark and hadrons coexist (also known as a mixed phase) [30]. There are also models of smooth crossover transition from the hadron to the quark phase described by the chiral mean-field model [16,31], where also at high temperature soluted quark in the hadron phase and soluted hadron in the quark phase can occur. Therefore, although the presence of strange stars is ruled out, the debate of whether QM can exist at the cores of NSs is not settled.

The deconfinement transition most probably happens during the formation of NSs after a supernova or after a BNSM. However, it can even occur in cold NSs initiated by a density

* mallick@iiserb.ac.in

change at the star core [24,25]. The PT can have all sorts of observable signatures, starting from GW to neutrino emission. As pulsars have misalignment between the rotation and the body symmetry axis [32,33], the tilt angle will also change during the PT. Therefore, during the PT of nuclear matter (NM) to QM at NS cores, multisignal astronomy comes to the forefront.

Phase transition in NSs has been a subject of scrutiny for a long time. There has been much literature discussing the process and nature of PTs [23–25,34–42]. One of the models for this PT is a two-step PT where NM is first deconfined to up and down QM [also known as two-flavor (2f) QM] [23–25,39,43]. The next step is converting excess down to strange quarks for the QM to attain stability [three-flavor (3f) matter]. The weakly interacting conversion of down to strange quarks generates a massive amount of neutrino-antineutrino pairs which come out of the star and account for the neutrino emission [44–48].

The process of PT is challenging to observe directly as it happens at the core of the NS, which is hidden from direct observation. However, there can be indirect observational signatures like the short rapid bursts of GW signals [24,25,39] accompanied by a neutrino signal. There can be an additional signature in the form of tilt angle evolution. As the NS converts to a quark star (QS) (sometimes also called a hybrid star due to the presence of both QM and NM), the star becomes more compact, and therefore the tilt axis of the star changes. As the PT is quite fast, the tilt angle also evolves quickly. Therefore, a sudden change of any observed pulsar’s tilt angle can be thought to be the signature of a PT happening at NS cores.

This article studies the multiple observable signatures associated with nuclear to quark transition in NSs. The multiple signals comprise GW signals, tilt angle evolution, and neutrino emission from the star. Section II describes our formalism for the multisignal observation from the NS to QS conversion: the neutrino energy deposition and the tilt angle evolution. Results of the multiple observables are discussed in Sec. III, and finally, in Sec. IV, we summarize our results and draw conclusions from them.

II. FORMALISM

Combustion in a NS due to shock is a two-step process: a sudden density fluctuation at the NS core which initiates a shock and deconfines NM to 2f QM; because 2f QM is unstable, it gains stability by converting to 3f QM. In our work, we considered the PT process where there is an abrupt jump in the density from hadron to quark phase (also known as Maxwell’s construction).

The first step of conversion from NM to 2f QM is swift and happens at the time scale of strong interaction [24,25]. Most of the observable signatures like neutrino emission and

tilt angle evolution come from the second process (the 2f-3f conversion), and in this work, we primarily study these aspects. In the second process, the excess of down (d) quarks convert to strange (s) quarks as long as the chemical potential of the down quarks exceeds that of the strange quarks and makes 3f matter via weak decays [39]. The conversion from NM to 3f QM occurs until the point where QM is more stable than the NM, and therefore we have a star that has stable 3f QM at the core and a NM outer surface.

A. Neutrino energy deposition

As the combustion front for the 2f-3f PT travels from the center to the surface of the star, at each time interval dt , the combustion front moves a distance dr with a velocity v [39]. At each instance $t = t_{ins}$, we have a shell of radius $r = r_{ins}$ from which neutrinos and antineutrinos are being formed and get annihilated, releasing energy in the process. We define the “neutrinosphere” R_n as the mean free path of the ν_e - $\bar{\nu}_e$ collision.

Taking r_{ins} to be the instantaneous neutrinosphere evolving with time, the energy deposition rate per unit volume at some distance r due to the neutrinosphere, $R_n = r_{ins}$ ($r > R_n$), is defined as [45,49]

$$\frac{d\Sigma}{dt} = \iint f_\nu(p_\nu, r) f_{\bar{\nu}}(p_{\bar{\nu}}, r) [\Lambda(\sigma, v_\nu, v_{\bar{\nu}}, \varepsilon)] d^3 p_\nu d^3 p_{\bar{\nu}}, \quad (1)$$

where f is the number density of the neutrinos in momentum space, p is the momentum of the neutrinos, and Λ is a function which depends on the cross section of the ν_e - $\bar{\nu}_e$ collision σ , the velocity of the neutrinos v_ν , $v_{\bar{\nu}}$, and the neutrino energies ε . The subscripts ν and $\bar{\nu}$ stand for neutrino and antineutrino, respectively. Each ν_e and $\bar{\nu}_e$ has a solid angle of emission, Θ . The momentum thus can be written as $p_\nu = \varepsilon_\nu \Theta$ and the volume element as $d^3 p_\nu = \varepsilon_\nu^2 d\varepsilon_\nu d\Theta$. The momentum integral thus decomposes into an energy integral $A(T)$ and angular integral $B(r, \theta)$ [50], where $A(T)$ is a function of the temperature T of the neutrinosphere and $B(r, \theta)$ is the function of the path taken by the ν_e and $\bar{\nu}_e$ to escape from the neutrinosphere. The energy with which each ν_e and $\bar{\nu}_e$ is emitted depends on the temperature of the neutrinosphere. The functions A and B can be calculated by assuming the metric of a slowly rotating star [51],

$$ds^2 = -e^{2\nu(r,\theta)} dt^2 + e^{2\lambda(r,\theta)} dr^2 + e^{2\mu(r,\theta)} d\theta^2 + e^{2\psi(r,\theta)} [d\phi - \omega(r) dt]^2 \quad (2)$$

and solving them numerically [51–53], where ν , λ , ψ , and μ are unknown functions of r and θ .

The deflection angle of emission of neutrinos is then calculated from the null geodesics [45,49] at the equatorial region and the expression for $B(r, \pi/2)$ is given by

$$B(r, \pi/2) = \frac{2\pi^2}{3} [6 + \Upsilon(r) + 4\sqrt{1 + \Upsilon(r)}][\sqrt{1 + \Upsilon(r)} - 1]^4, \quad (3)$$

where

$$\Upsilon(r)|_{\theta=\pi/2} = \frac{e^{4\psi(R_n)-2\psi(r)}(-e^{2\nu(r)} - e^{2\psi(r)}\omega(r)^2)}{(e^{2\psi(R_n)}(\omega(r) - \omega(R_n)) + \sqrt{e^{2(\nu(R_n)+\psi(R_n))} + e^{4\psi(R_n)}\omega(R_n)^2})^2}. \quad (4)$$

Thus, B defines the path of the neutrino emission. The function $A(T)$ is evaluated by integrating $f_\nu(p_\nu, r)f_{\bar{\nu}}(p_{\bar{\nu}}, r) \varepsilon_\nu^2 \varepsilon_{\bar{\nu}}^2 [\Lambda(\sigma, \nu, \varepsilon)] d\varepsilon_\nu d\varepsilon_{\bar{\nu}}$ over the energies and we get [45,54]

$$A(T) \propto (k_B T(r))^9. \quad (5)$$

The temperature T at the neutrinosphere can be written in terms of the luminosity at infinity, $L(r \rightarrow \infty)$. The temperature T at the neutrinosphere can be written as a function of temperature $T(r)$ at some distance r . Thus the energy deposition rate per unit volume for neutrinos is given by

$$\begin{aligned} \frac{d\Sigma}{dt} &= \kappa \left[\left(\frac{e^{2\nu(R_n)} + e^{2\psi(R_n)}\omega(R_n)^2}{e^{2\nu(r)} + e^{2\psi(r)}\omega(r)^2} \right)^{9/2} \right. \\ &\quad \times \left. \left(\frac{L(r \rightarrow \infty)}{\pi R_n^2 \sigma e^{2\nu(R_n)} + \pi R_n^2 \sigma e^{2\psi(R_n)}\omega(R_n)^2} \right)^{9/4} \right] \\ &\quad \times \left[6 + \Upsilon(r) + 4\sqrt{1 + \Upsilon(r)} \right] \left[\sqrt{1 + \Upsilon(r)} - 1 \right]^4. \end{aligned} \quad (6)$$

B. Tilt evolution

If we assume some asymmetry (due to a poloidal magnetic field) in our star, then the free precision model [32,33] gives rise to a misalignment χ between the rotation and the asymmetry axis (here the magnetic axis) which models a pulsar. The moment of inertia for such a system can be written as

$$I_{ij} = I_0 \delta_{ij} + \Delta I \left(n_i n_j - \frac{\delta_{ij}}{3} \right), \quad (7)$$

where the unit vector $n_i = (0, 0, 1)$ points in the direction of the asymmetry axis. The two principal moments $I_1 = I_2$ are equal and the third moment defines the asymmetry: $\Delta I = I_3 - I_1$. Thus I_0 is the moment of inertia for the spherical symmetric case when $I_1 = I_2 = I_3$ and $\Delta I = 0$. Thus in general if the angular velocity of the star is $\Omega_i = (\Omega_1, \Omega_2, \Omega_3)$ then we can calculate the angular momentum as

$$J_i = I_{ij} \Omega_j = \left(I_0 - \frac{1}{3} \Delta I \right) \Omega_i + \Delta I \Omega_3 n_i. \quad (8)$$

The angle between J_i and n_i is the misalignment angle of the star, χ . During the PT, along with the neutrino emission the star also loses energy. The total amount of energy released from such a misaligned star as the misalignment angle evolves from χ_1 to χ_2 is given by

$$E = \int_{\chi_1}^{\chi_2} \frac{dJ}{dt} d\chi. \quad (9)$$

In general the energy loss equation can be written as $\frac{dE}{dt} = \frac{\partial E}{\partial \chi} \Big|_{J} \frac{d\chi}{dt} + \frac{\partial E}{\partial J} \Big|_{\chi} \frac{dJ}{dt}$, where Eq. (9) can be inverted and using

Eq. (8) we can write [55]

$$\dot{\chi} = \frac{\dot{E}}{I\Omega^2} \cot \chi, \quad (10)$$

where $\dot{E} = \dot{E}_{PT} + \dot{E}_{vis}$ and \dot{E}_{PT} and \dot{E}_{vis} are the energy loss due to the PT and viscosity, respectively. In our work, we are considering our star as a fluid, and thus viscous damping can occur as a mode of energy loss following the Euler equations apart from the PT energy loss. The energy loss, however, for such processes is in the time scale of years [55], and as the time scale of PT is on the order of milliseconds, the energy loss due to viscosity is neglected as the time scale for energy loss is several orders higher than milliseconds ($\dot{E}_{vis} \approx 0$). The evolution of angular momentum has been shown for the case of GW radiation loss [56] and for the magnetic radiation loss [55], and in the present work as the star loses energy due to PT, the torque generated in the process evolves the misalignment angle.

III. RESULTS AND DISCUSSIONS

We start our calculation with S271 [57,58] parameter setting to describe the NM and MIT bag model having quark interaction [59–61] to describe QM. These EoS are in agreement with the current nuclear and astrophysical bounds [9,62,63]. The 2f matter consists only of up and down quarks (with masses 2 and 5 MeV, respectively), whereas the 3f QM additionally has strange quarks in it of mass 95 MeV. The bag constant is taken to be $B^{1/4} = 140$ MeV, and the quark coupling value a_4 is 0.5. One of the physical processes by which QM can seed inside a cold NS is by spin down. With our choice of EoS, the QM becomes more stable than the hadronic matter at a pressure of about 6×10^{34} dyn/cm², which is about three times the nuclear saturation density. For a $1.6M_\odot$ star, this happens between 860 and 800 Hz frequency as shown in Fig. 1. Therefore, after its birth, a $1.6M_\odot$ NS is rapidly rotating (more than 1000 Hz frequency). As it cools and settles down, it loses its rotational energy to electromagnetic radiation and slows down. The QM core appears at the center after its frequency becomes less than 860 Hz.

The deconfinement of NM to 2f QM is almost instantaneous; however, the 2f to 3f conversion is relatively slow. Most of the observable signature comes from the second process. Keeping the baryonic mass M_B constant, the 2f star rotating with 50 Hz evolves to a 3f star via the weak interaction. The 3f star has a higher central density, a smaller radius, and a slightly larger rotational velocity than the 2f star. The star heats up during the PT and attains a temperature of about 0.1–1 MeV [39]. The T does not affect the EoS significantly but governs the diffusion dynamics of the 2f to 3f quark conversion. At $T \approx 10^{-1}$ MeV, the neutrinosphere velocity remains comparable to the combustion front velocity, and we can identify the neutrinosphere with the combustion front [39]. Using

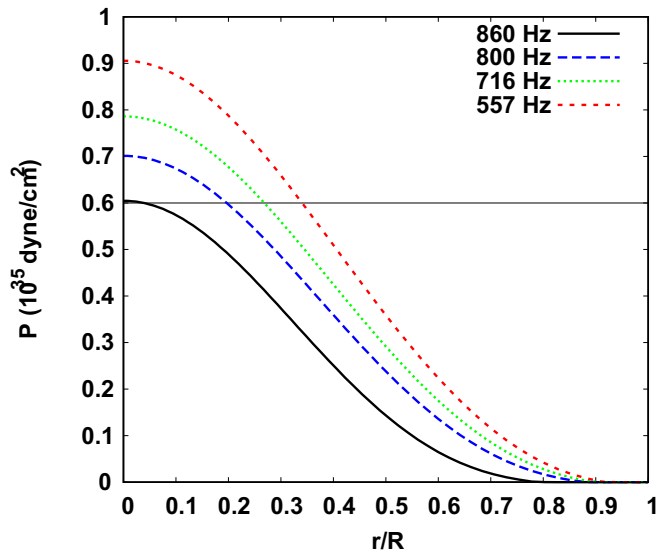


FIG. 1. The figure shows the spin down of a $1.6M_{\odot}$ star from 860 to 557 Hz as the central pressure of the star increase. The horizontal line of pressure 6×10^{34} dyn/cm² indicates the point from where QM becomes more stable than hadronic matter.

the combustion front velocity, we find the star's density profile changes as a function of time as 2f matter settles into 3f QM. A stable intermediate star ensuring conservation of baryonic mass is obtained, which has 3f matter from the center to the front location, followed by metastable 2f matter and then NM at the outer region. The conversion velocity increases from the center to the star's surface, and its magnitude is of the order of $\approx 10^{-2}$ times the speed of light [39]. It takes about a few tens of milliseconds for the PT process to happen. Also, the combustion of 3f matter happens up to the point where 3f matter is more stable than NM and which can be deduced from the respective chemical potential of NM and 3f QM as a function of pressure. For a given pressure, the phase with the least chemical potential is considered to be the stable state of matter at that pressure. Therefore, at higher pressure (corresponding to higher density), QM is the stable state, whereas at lower pressure (corresponding to lower density), the nuclear matter is the stable state. Therefore, in a star, the core region is in the quark phase, and the outer region of the star is in the nuclear phase, and we thereby obtain a hybrid star [39].

The total energy deposition rate is calculated by numerically integrating Eq. (6) from $t(r_i) = 0$ to $t(r_f) = t_f$ by using the profile of each intermediate star for each time instant. Here r_i and r_f are the initial and final radii of the combustion front (neutrinosphere), and t_f is the final time for the PT. The neutrinos are emitted and annihilated from the entire volume of the 3f matter, and thus the total energy deposition rate is calculated by integrating $d\Sigma/dt$ over the entire volume of the 3f matter of the star. However, the star has an asymmetry whose information lies in the function B and governs the path taken for neutrino emission; thus, integrating over the entire volume is restricted, but the energy information lies in the function A , which is independent of the asymmetry of our star. An order of approximate calculation for the total energy

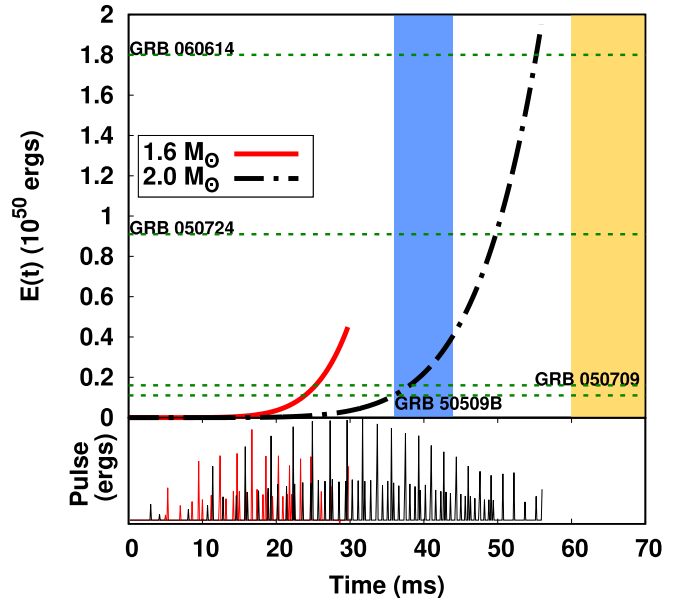


FIG. 2. Energy deposition rate on the surface of the QS plotted as a function of time. The y axis of the top section shows the total amount of energy deposited on the star's surface at that instant in time. The bottom section shows the spectrum of the pulse emitted in ergs as a function of time. The total energy has been normalized by 10^{50} ergs. At $t = 29.7$ and 55.9 , the value of $E(t)$ gives the total energy that has been emitted throughout the process for $1.6M_{\odot}$ and $2.0M_{\odot}$ stars, respectively. E_{iso} and t_{90} for a few GRBs are shown as references for the energy and time scale of typical millisecond bursts. The vertical columns indicate the error in the measurement of the observed t_{90} .

deposition rate dE/dt can thus be evaluated by approximating the integral $dE/dt = \int [d\Sigma/dt] dV \approx [d\Sigma/dt] \frac{4}{3} \pi R_*^3$, where R_* is the average radius of the 3f star.

The total energy deposition rate is plotted as a function of time in the top panel of Fig. 2. The y axis shows the amount of energy deposited on the star's surface by the neutrinos generated by weak combustion at the neutrinosphere at that particular time. The total energy deposited is shown in Table I. As the mass of the star increases, the time taken to convert 2f to 3f matter increases [39]. Thus, more neutrinos are emitted from massive stars, and the probability of collision of neutrino-antineutrino pairs increases; thus, the energy deposition increases. It is seen that the energy deposited is in the range 10^{49} – 10^{50} ergs, and the time scale for the process lies between 29.7 and 55.9 ms. The bottom panel of Fig. 2 shows the energy emitted by each intermediate star at that particular instant of time. The neutrino annihilation process can be seen in the simulation snapshot in Fig. 3. The peak of the neutrino opacity increases with an increase in density and is quite significant at around a density of $\approx 5 \times 10^{14}$ g/cm³ for temperature $T = 0.5$ MeV [64]. This corresponds to a radius of ≈ 1 km, which remains opaque to neutrinos and prevents significant neutrino flow from the star center. It has also been shown that the opacity decreases with an increase in temperature. Our PT energies for neutrino emission are in the scale of $T = 0.1$ MeV, for which the opaque radius is even

TABLE I. The energy deposition $E(t)$, the final time taken for the PT, t_f , and continuous and phase-transition gravitational waves (CGW and PTGW [39]) for a source at a distance of 2 kpc, 100 kpc, and 1 Mpc. The tabulation has been done for three masses of the star, $1.6M_\odot$, $1.8M_\odot$, and $2.0M_\odot$, and for an initial frequency of 50 Hz. The final frequency of the star after PT is also shown.

Mass (M_\odot)	$E(t = t_f)$ (ergs)	t_f (ms)	CGW (h_0 at $l = 2$ kpc)	PTGW (h_0 at $l = 2$ kpc)	CGW/PTGW (h_0 at $l = 100$ kpc)	CGW/PTGW (h_0 at $l = 1$ Mpc)	Ω final (Hz)
1.6	4.49×10^{49}	29.7	2.14×10^{-27}	$\approx 10^{-21}$	$\approx 10^{-29}/10^{-23}$	$\approx 10^{-30}/10^{-24}$	51.79
1.8	4.97×10^{49}	30.7	2.02×10^{-27}	$\approx 10^{-20}$	$\approx 10^{-29}/10^{-22}$	$\approx 10^{-30}/10^{-23}$	52.82
2.0	1.95×10^{50}	55.9	1.78×10^{-27}	$\approx 10^{-19}$	$\approx 10^{-29}/10^{-21}$	$\approx 10^{-30}/10^{-22}$	56.53

higher and corresponds to ≈ 2 km, ensuring the restriction of free streaming neutrinos. Also, the neutrinos are emitted to a radius up to which the PT to 3f matter occurs, and for a $1.6M_\odot$ star, its value along the equatorial direction is 10.27 km (equatorial radius of the star being 13.07 km), and for a $2M_\odot$ star it is 10.72 km (equatorial radius being 12.42 km).

Astrophysically, many short γ -ray burst (SGRB) events have been detected [65,66]. The energy budgets of SGRB events such as GRB 050509B (at $z \approx 0.225$, $E_{iso} \approx 1.1 \times 10^{48} k$ ergs, where k ranges from 1 to 10, $t_{90} \approx 40 \pm 4$ ms) [67,68], GRB 060502B (at $z \approx 0.287$, $E_{iso} \approx 8.0 \times 10^{48}$ ergs) [69], GRB 050709 (at $z \approx 0.16$, $E_{iso} \approx 1.6 \times 10^{49}$ ergs, $t_{90} \approx 70 \pm 10$ ms) [70], and GRB 060614 (at $z \approx 0.125$, $E_{iso} \approx 1.8 \times 10^{50}$ ergs) have been calculated, where E_{iso} is the isotropic equivalent radiated energy in the rest frame of the source and t_{90} is the time duration in which 90% of the photons detected are emitted from the source [71]. A possible source of such SGRBs has been credited to NS-NS mergers, where the energy and time signatures from the models fall within the observed limit. The energy and time signatures

of neutrino-antineutrino annihilation from the PT process, as described by our model, fall well within the observed limit. However, more rigorous calculations in the direction of variability, spectral hardness, and the correlation between the peak energy and isotropic luminosity are required to establish a strong connection with SGRBs [72,73]. We plan to do such a detailed calculation in the future.

As the NS loses a considerable amount of energy due to the 2f-3f conversion over a period of time, the NS's misalignment angle evolves accordingly [Eq. (10)]. The evolution of the misalignment angle for a NS is plotted as a function of time in Fig. 4. The y axis of the plot shows the change in the misalignment angle χ with respect to some initial angle χ_0 . Thus the change $\Delta\chi$ is defined as $\Delta\chi \equiv \chi - \chi_0$. It can be seen from Fig. 4 that the value of $\Delta\chi$ takes negative values; that is, the misalignment angle decreases as energy is being emitted from the star. The star could reach alignment if the initial angle χ_0 is smaller than $\pi/9$. The previous spin-down model which uses magnetic braking predicts alignment ranging from a few seconds to years [55]. However, in our model, the time scales

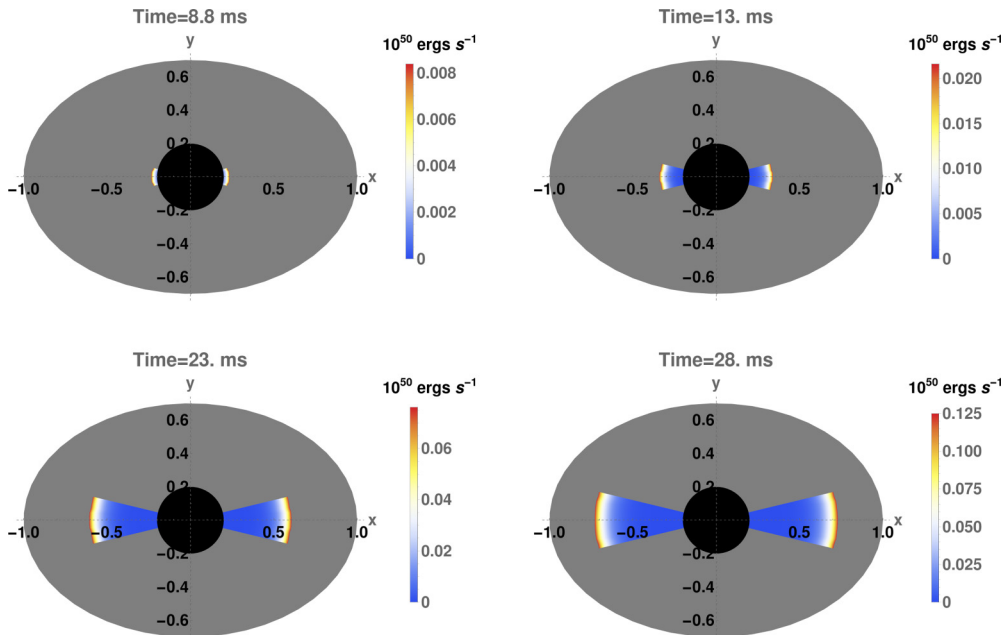


FIG. 3. Snapshot of simulation of the dynamic evolution of neutrino and antineutrino escape and annihilation. At each snapshot, the neutrino and antineutrino can be seen to be produced due to PT and get annihilated. The corresponding energy deposited on the surface at each radius is shown as a heat map. The simulation only shows deposition along $\theta = \pi/2$ (equatorial region); however, the total energy is emitted from the entire volume of the star. The dark sphere is the opaque region for neutrinos.

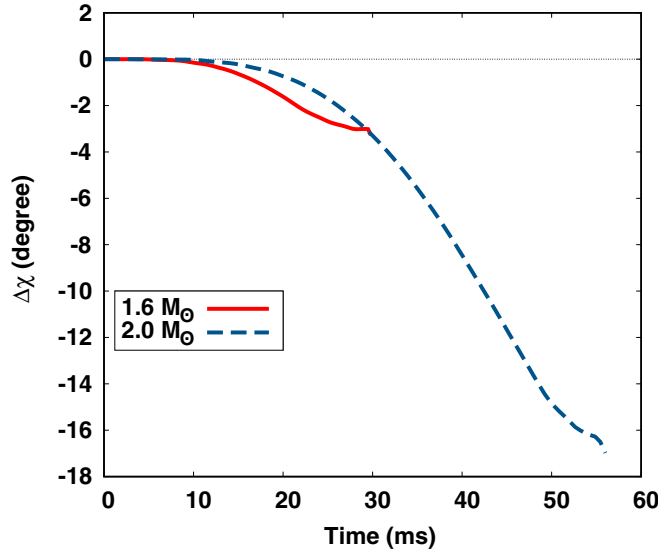


FIG. 4. Misalignment angle evolution due to energy emitted from the star for two different masses. The misaligned angle is seen to be decreasing and going towards alignment. The more massive star has a higher probability of attaining alignment than the lower mass star. Here the initial angle is taken to be $\pi/5$ (36°).

are in milliseconds and are entirely due to the PT. Thus the PT can, in general, quicken the alignment process of a misaligned star. The slope for the evolution of $\Delta\chi$ changes as the mass of the star increases. This is because the peak of the energy loss shifts both in magnitude and time as the mass increases (bottom panel of Fig. 2). Thus, more massive stars have a higher probability of getting aligned.

The PT process brings about a change in the interior of the star. The density evolution during the settling of a $2f$ star to a stable $3f$ star leads to quadrupole moment variation, leading to GW emission directly from the PT process itself, calculation of which is done in our latest work [39]. The GW strain comes out to be of the order of 10^{-23} – 10^{-21} for a source located at 1 Mpc distance, and the amplitude spectrum calculation reveals peaks in the 1–3 kHz range. In this work, we provided the overall picture of possible GW emission, focusing on the continuous GW emission. Due to misalignment, an initial NS and final QS emit continuous GW (CGW) signals, separated by a short-lived signal originating from the PT (PTGW). The continuous GW signal evolves with the misalignment angle's evolution of the star. The h_+ polarization [74] is given by

$$h_+ = h_0 \sin \chi \left[\frac{1}{2} \cos \chi \sin i \cos i \cos \Omega t - \sin \chi \frac{1 + \cos^2 i}{2} \cos 2\Omega t \right], \quad (11)$$

where $h_0 = \frac{4G}{c^4} \frac{I \epsilon}{l} \Omega^2$, i is the line of sight inclination, ϵ is the ellipticity of the star, and l is the radial distance of the NS from the Earth. We perform the GW calculation assuming that the source star at a distance $l = 2$ kpc (similar distance to the Crab Pulsar) from the Earth and at an inclination angle of $i = 30^\circ$ and the ellipticity of the NS and QS is taken to be 10^{-4}

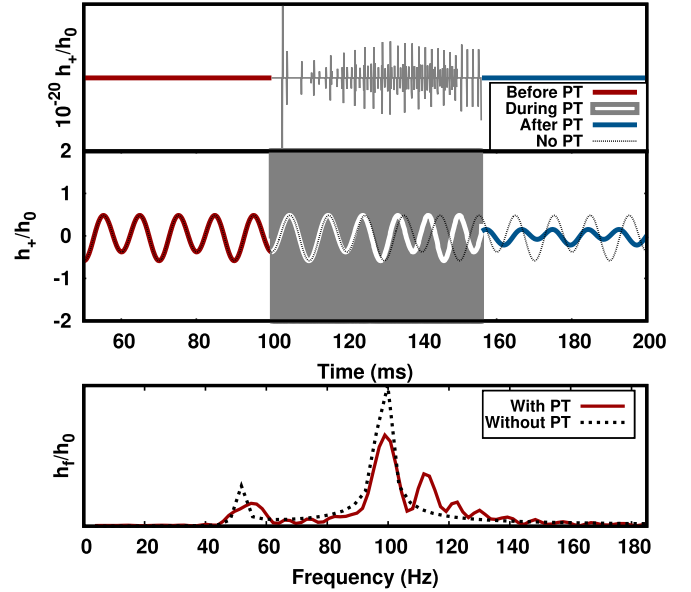


FIG. 5. Top: The GW signal template emitted from rotating NSs due to PT. The y axis shows the h_+ polarization of the GW normalized with the amplitude h_0 . The distance from the Earth's surface is taken to be 2 kpc, and the line of sight angle is taken to be 30° . The first, second, and third GW plots are for a $2.0M_\odot$ star where the amplitude is shown for regions before, during, and after PT with no PT amplitude in the background for reference. Bottom: The spectral decomposition of the continuous emission of GW, indicating peaks in the different frequency regions as the PT evolves as compared to no PT.

[74]. The total waveform consists of continuous GW signals emitted from the NS and QS, respectively (of the order of 10^{-27} and changing with the evolution of misalignment angle due to PT) separated by a GW signal from the PT process itself (of the order of 10^{-19}) (upper panel of Fig. 5).

The continuous GW changes both in amplitude and frequency. The amplitude decreases with a decrease of $\Delta\chi$ as it moves towards alignment. The frequency increases because, after the PT, the QS becomes smaller due to the softening of the equation of state; hence, the angular velocity increases. The change in frequency can be seen from the bottom panel of Fig. 5, where spectral decomposition of the continuous GW wave strain is done. In the absence of the PT, we have peaks for two primary frequencies of the GW, a combination of Ω and 2Ω [Eq. (11)]. However, for the PT, frequency peaks other than Ω and 2Ω can be seen. As the star spins up, one has peaks at different frequencies, indicating a PT. Different signals from the PT for a star with initial $\Omega = 50$ Hz, $l = 2$ kpc, and $h_0 = 2.38 \times 10^{-27}$ are tabulated in Table I. However, in general, the h_0 for continuous GWs ranges between 10^{-27} and 10^{-31} depending on the distance of the source from the Earth's surface. For the present detectors, the continuous GW signals are still beyond detection capability; such strains can be extracted from the experiments such as the Einstein@Home all-sky search for periodic GWs, which was an all-sky search [75] in the frequency range 50–1190 Hz, where the raw data were collected for a long period of time and then the weak

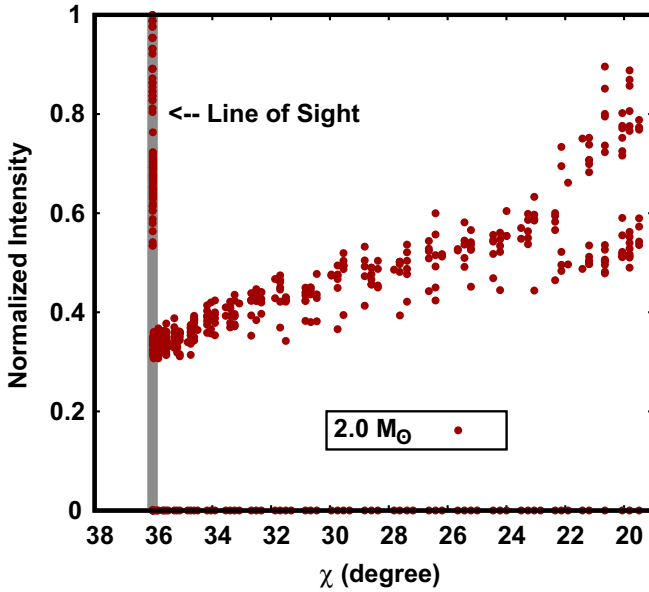


FIG. 6. Normalized intensity of radio emission from a $2.0M_{\odot}$ radio pulsar plotted with respect to the evolution of the misalignment angle of the pulsar. The P for the pulsar evolves from 20.0 to 17.69 ms in 55.9 ms of PT time. The intensity drops sharply as the misalignment angle passes through the line of sight [here from $\chi = \pi/5$ (36°) to $\chi = 10\pi/51$ (35°)] and then the intensity is seen to be increasing due to gain in rotational velocity [for $\chi = 10\pi/51$ (35°) to $\chi = 10\pi/95$ (19°)]. This can cause the pulsar signal to disappear or appear depending on the line of sight.

continuous GW was extracted from the background noise using the Hugo-transform method. The study concluded a strain upper bound of $h_0 \approx 7.6 \times 10^{-25}$ at 152 Hz, and with more data added, it can find an even fainter signal similar to the order of strain that the model predicts pre- and post-PT.

The short-burst GWs from our model for $T = 0.1$ MeV and sources ≈ 100 kpc and ≈ 1 Mpc can be seen from Table I. The amplitude of the GW signal falls well within the Advanced LIGO and Advanced Virgo detection with amplitude strain of the order of 10^{-23} and frequency bandwidth of 30 Hz to 2 kHz, which roughly defines the detector capability and noise curve.

The change in misalignment angle is also reflected in the evolution of radio intensity from radio pulsars. The intensity from pulsars due to the presence of a magnetosphere is given by [76]

$$I_{\text{norm}} = P^{q-4} \dot{P} \cos^2 \chi f^{q-3} \rho^{2q-6}, \quad (12)$$

where I_{norm} is the normalized intensity, P and \dot{P} are the period and the period derivative of the pulsar, and the parameter f indicates the ratio of the maximum altitude of an open field line with respect to the light cylinder radius, which is taken to be ≈ 3 , and ρ is the angle between the emission points and magnetic moment, which is taken to be 1° . The emission follows a power-law expression l^q for emission from a radial distance l . For curvature-radiation emitting radio waves, the parameter q is taken to be -0.5 [77]. The normalized intensity I_{norm} is plotted in Fig. 6 as a function of the misalignment

angle χ . The misalignment axis is taken to be initially coinciding with the line of sight. During the PT, as the misalignment angle evolves, the intensity falls sharply and goes out from the line of sight; however, because the star gains angular velocity, the intensity of the radio pulsar increases again outside the line of sight to values similar to its original intensity. Thus, a pulsar may disappear from view after the PT due to much decrease in intensity. However, the opposite may also happen, and pulsars that were not visible before could evolve and cross the line of sight due to increased intensity and may become visible.

IV. SUMMARY AND CONCLUSION

The PT in NSs involves deconfinement of NM to 2f matter followed by weak combustion from 2f to 3f matter. As the combustion front evolves with time, the neutrino-antineutrino pairs are generated, annihilating and depositing energy on the star's surface. As the star loses energy due to the PT, it undergoes physical changes such as misalignment angle evolution and rotational velocities. Thus, the phenomena of PT in NSs can be captured by studying the multiple signals coming from NSs, like the neutrino energy deposition, evolution of the star misalignment axis, and emission of GWs.

Due to the generation of neutrinos during weak combustion, a massive amount of energy is deposited at the star's surface. The total energy deposited by the star is around 10^{49} - 10^{50} ergs at time scales of the order of tens of milliseconds. Due to the energy loss, the star's tilt angle can evolve up to $\pi/15$ (12°), thus evolving towards alignment. The misalignment angle changes are reflected in the continuous emission of GWs whose amplitude is of the order of 10^{-27} - 10^{-31} . The amplitude and frequency of the GW signature change during PT due to a change in misalignment angle and rotational frequency. The actual process of PT has much stronger signals (amplitude is of the order of 10^{-20} - 10^{-21}) and lasts at a maximum for a few tens of milliseconds.

Our model's energy budget and time duration fall within the observed SGRB limits. However, a more detailed study of other features of γ rays from our PT model is needed for them to be considered as a source of SGRBs. Although the continuous GW signals are beyond the present operating detectors' capabilities, the strong GW burst signal from the PT process itself is well within detection capability. GWs originating from the observed direction of neutrinos and γ rays could point towards PT from NSs to QSs. The sudden disappearance or appearance of radio emissions from particular pulsars emitting γ rays and having short but strong GW signals would predict astrophysical PTs.

Our PTGW amplitude is an order-and-a-half magnitude lower than the GW signal detected from BNSM GW170817, and the frequency is also an order higher. In comparison to supernova events, our energy budget matches closely with the energy release of type II-P supernova events. In our present study, we study the PT process in a cold NS. However, such a PT process is more likely to occur in hypermassive NSs in BNSMs and proto-neutron stars after a supernova. Our present endeavor is to study the two-step PT of NM to QM happening in such astrophysical theaters.

ACKNOWLEDGMENTS

D.K. thanks CSIR-HRDG (Council of Scientific and Industrial Research-Human Resource Development Group), Government of India, for financial support. R.M. is grateful to the SERB (Science and Engineering Research Board), Government of India, for monetary support in the form of the

Ramanujan Fellowship (SB/S2/RJN-061/2015). R.P. would like to acknowledge the financial support in the form of INSPIRE fellowship provided by DST (Department of Science and Technology), India. S.S., R.M., R.P., and D.K. would also like to thank IISER Bhopal for providing all the research and infrastructure facilities.

-
- [1] E. V. Shuryak, *Phys. Rep.* **61**, 71 (1980).
 [2] M. Gyulassy and L. McLerran, *Nucl. Phys. A* **750**, 30 (2005).
 [3] A. Andronic, P. Braun-Munzinger, K. Redlich, and J. Stachel, *Nature (London)* **561**, 321 (2018).
 [4] J. M. Lattimer and M. Prakash, *Science* **304**, 536 (2004).
 [5] P. de Forcrand, *PoS (LAT2009)*, 010 (2010).
 [6] P. B. Demorest, T. Pennucci, S. M. Ransom, M. S. E. Roberts, and J. W. T. Hessels, *Nature (London)* **467**, 1081 (2010).
 [7] J. Antoniadis *et al.*, *Science* **340**, 1233232 (2013).
 [8] H. T. Cromartie *et al.*, *Nat. Astron.* **4**, 72 (2019).
 [9] B. P. Abbott *et al.* (LIGO Scientific and Virgo Collaborations), *Phys. Rev. Lett.* **119**, 161101 (2017).
 [10] T. Hinderer, B. D. Lackey, R. N. Lang, and J. S. Read, *Phys. Rev. D* **81**, 123016 (2010).
 [11] J. S. Read, C. Markakis, M. Shibata, K. Uryu, J. D. E. Creighton, and J. L. Friedman, *Phys. Rev. D* **79**, 124033 (2009).
 [12] W. Del Pozzo, T. G. F. Li, M. Agathos, C. Van Den Broeck, and S. Vitale, *Phys. Rev. Lett.* **111**, 071101 (2013).
 [13] M. Agathos, J. Meidam, W. Del Pozzo, T. G. F. Li, M. Tompitak, J. Veitch, S. Vitale, and C. Van Den Broeck, *Phys. Rev. D* **92**, 023012 (2015).
 [14] K. Chatziioannou, C. J. Haster, and A. Zimmerman, *Phys. Rev. D* **97**, 104036 (2018).
 [15] E. Annala, T. Gorda, A. Kurkela, and A. Vuorinen, *Phys. Rev. Lett.* **120**, 172703 (2018).
 [16] E. R. Most, L. R. Weih, L. Rezzolla, and J. Schaffner-Bielich, *Phys. Rev. Lett.* **120**, 261103 (2018).
 [17] R. Nandi and S. Pal, *Eur. Phys. J. Spec. Top.* **230**, 551 (2021).
 [18] N. B. Zhang, B. A. Li, and J. Xu, *Astrophys. J.* **859**, 90 (2018).
 [19] A. Bauswein, N.-U. F. Bastian, D. B. Blaschke, K. Chatziioannou, J. A. Clark, T. Fischer, and M. Oertel, *Phys. Rev. Lett.* **122**, 061102 (2019).
 [20] N. Itoh, *Prog. Theor. Phys.* **44**, 291 (1970).
 [21] E. Witten, *Phys. Rev. D* **30**, 272 (1984).
 [22] A. R. Bodmer, *Phys. Rev. D* **4**, 1601 (1971).
 [23] A. Bhattacharyya, S. K. Ghosh, P. S. Joarder, R. Mallick, and S. S. Raha, *Phys. Rev. C* **74**, 065804 (2006).
 [24] R. Prasad and R. Mallick, *Astrophys. J.* **859**, 57 (2018).
 [25] R. Prasad and R. Mallick, *Astrophys. J.* **893**, 151 (2020).
 [26] D. Kuzur *et al.*, *J. Phys. G: Nucl. Part. Phys.* **47**, 105203 (2020).
 [27] L. Bonanno and A. Sedrakian, *Astron. Astrophys.* **539**, A16 (2012).
 [28] B. Holdom, J. Ren, and C. Zhang, *Phys. Rev. Lett.* **120**, 222001 (2018).
 [29] M. Herzog and F. K. Ropke, *Phys. Rev. D* **84**, 083002 (2011).
 [30] N. K. Glendenning and S. A. Moszkowski, *Phys. Rev. Lett.* **67**, 2414 (1991).
 [31] V. Dexheimer, *Pub. Astron. Soc. Aust.* **34**, E066 (2017).
 [32] D. I. Jones and N. Andersson, *Mon. Not. R. Astron. Soc.* **324**, 811 (2001).
 [33] D. Kuzur and R. Mallick, *J. Astrophys. Astron.* **42**, 87 (2021).
 [34] A. Drago, A. Lavagno, and I. Parenti, *Astrophys. J.* **659**, 1519 (2007).
 [35] I. Mishustin, R. Mallick, R. Nandi, and L. Satarov, *Phys. Rev. C* **91**, 055806 (2015).
 [36] R. Mallick and M. Irfan, *Mon. Not. R. Astron. Soc.* **485**, 577 (2019).
 [37] R. Mallick and A. Singh, *Int. J. Mod. Phys. E* **27**, 1850083 (2018).
 [38] A. Olinto, *Phys. Lett. B* **192**, 71 (1987); *Nucl. Phys. B* **24**, 103 (1991).
 [39] R. Mallick, S. Singh, and R. Prasad, *Mon. Not. R. Astron. Soc.* **503**, 4829 (2021).
 [40] M. G. Alford, S. Han, and K. Schwenzer, *Phys. Rev. C* **91**, 055804 (2015).
 [41] B. Niebergal, R. Ouyed, and P. Jaikumar, *Phys. Rev. C* **82**, 062801(R) (2010).
 [42] A. Drago and G. Pagliara, *Phys. Rev. C* **92**, 045801 (2015).
 [43] A. Bhattacharyya, S. K. Ghosh, R. Mallick, and S. Raha, *Phys. Rev. C* **76**, 052801(R) (2007).
 [44] R. Mallick, A. Bhattacharyya, S. K. Sanjay, and S. Raha, *Int. J. Mod. Phys. E* **22**, 1350008 (2013).
 [45] Z. Kovacs, K. S. Cheng, and T. Harko, *Mon. Not. R. Astron. Soc.* **402**, 1714 (2010).
 [46] A. Bhattacharyya, S. K. Sanjay, and S. Raha, *Phys. Lett. B* **635**, 195 (2006).
 [47] S. K. Ghosh, S. C. Phatak, and P. K. Sahu, *Nucl. Phys. A* **596**, 670 (1996).
 [48] J. D. Anand, A. Goyal, V. K. Gupta, and S. Singh, *Astrophys. J.* **481**, 954 (1997).
 [49] R. Mallick and S. Majumder, *Phys. Rev. D* **79**, 023001 (2009).
 [50] H. A. Bethe and J. R. Wilson, *Astrophys. J.* **295**, 14 (1985).
 [51] J. B. Hartle and K. S. Thorne, *Astrophys. J.* **153**, 807 (1968).
 [52] J. R. Oppenheimer and G. M. Volkoff, *Phys. Rev.* **55**, 374 (1939).
 [53] R. C. Tolman, *Phys. Rev.* **55**, 364 (1939).
 [54] K. Asano and F. Takeshi, *Astrophys. J.* **531**, 949 (2000).
 [55] S. K. Lander and D. I. Jones, *Mon. Not. R. Astron. Soc.* **481**, 4169 (2018).
 [56] C. Cutler and D. I. Jones, *Phys. Rev. D* **63**, 024002 (2000).
 [57] G. A. Lalazissis, J. Konig, and P. Ring, *Phys. Rev. C* **55**, 540 (1997).
 [58] C. J. Horowitz and J. Piekarewicz, *Phys. Rev. C* **66**, 055803 (2002).
 [59] M. Alford, D. Blaschke, A. Drago, T. Klähn, G. Pagliara, and J. Schaffner-Bielich, *Nature (London)* **445**, E7 (2007).
 [60] A. Chodos, R. L. Jaffe, K. Johnson, C. B. Thorn, and V. F. Weisskopf, *Phys. Rev. D* **9**, 3471 (1974).
 [61] S. Weissenborn, I. Sagert, G. Pagliara, M. Hempel, and J. Schaffner-Bielich, *Astrophys. J. Lett.* **740**, L14 (2011).
 [62] T. E. Riley *et al.*, *Astrophys. J. Lett.* **887**, L21 (2019).
 [63] M. C. Miller *et al.*, *Astrophys. J. Lett.* **887**, L24 (2019).

- [64] P. N. Alcain and C. O. Dorso, *Nucl. Phys. A* **961**, 183 (2017).
[65] E. Nakar, *Phys. Rep.* **442**, 166 (2007).
[66] J. Villasenor *et al.*, *Nature (London)* **437**, 855 (2005).
[67] N. Gehrels *et al.*, *Nature (London)* **437**, 851 (2005).
[68] J. S. Bloom *et al.*, *Astrophys. J.* **638**, 354 (2006).
[69] J. S. Bloom *et al.*, *Astrophys. J.* **654**, 878 (2007).
[70] D. B. Fox *et al.*, *Nature (London)* **437**, 845 (2005).
[71] J. D. Scargle, J. Norris, and J. Bonnell, *AIP Conf. Proc.* **428**, 181 (1998).
[72] T. Le and V. Mehta, *Astrophys. J.* **837**, 17 (2017).
[73] N. Gehrels and P. Meszaros, *Science* **337**, 932 (2012).
[74] S. Bonazzola and E. Gourgoulhon, *Astron. Astrophys.* **312**, 675 (1996).
[75] J. Aasi *et al.* (LIGO Scientific Collaboration and Virgo Collaboration), *Phys. Rev. D* **87**, 042001 (2013).
[76] H. G. Wang *et al.*, *Astrophys. J.* **789**, 73 (2014).
[77] M. A. Ruderman and P. G. Sutherland, *Astrophys. J.* **196**, 51 (1975).